

When Anderson localization makes quantum particles move backward

Tony Prat¹, Dominique Delande¹, Nicolas Cherroret¹

¹Laboratoire Kastler Brossel, UPMC-Sorbonne Universités, CNRS,
ENS-PSL Research University, Collège de France; 4 Place Jussieu, 75005 Paris, France
(Dated: 19/04/2017)

We unveil a novel and unexpected manifestation of Anderson localization of matter wave packets that carry a finite average velocity: after an initial ballistic motion, the packet center-of-mass experiences a retroreflection and slowly returns to its initial position. We describe this effect both numerically and analytically in dimension 1, and show that it is destroyed by weak particle interactions which act as a decoherence process. The retroreflection is also present in higher dimensions, provided the dynamics is Anderson localized.

PACS numbers: 72.15.Rn, 67.85.-d, 05.60.Gg

Anderson localization (AL), the absence of wave diffusion due to destructive interference in disordered potentials [1], is ubiquitous in condensed-matter systems, wave physics or atom optics. This offers many experimental platforms for its characterization, as was recently demonstrated experimentally with light [2, 3] (see however [4, 5]) or ultrasound waves [6]. Very recently, AL of atomic matter waves has also been observed [7–11], as well as its many-body counterpart [12, 13]. A precious asset of atom optics experiments is to allow for direct tests of fundamental manifestations of AL, such as the time evolution of wave packets. In this context, a common experimental scenario for probing localization consists in preparing a spatially narrow atomic wave packet in a trap, then opening the trap and recording the time evolution of the gas [14, 15]. After it has been released, the wave packet spreads symmetrically around its initial position and, after a transient ballistic expansion, quickly becomes localized in space. What happens, now, if a nonzero average velocity is additionally imprinted to the gas? In a naive picture, one expects the randomization of velocities due to scattering on the random potential to stop the initial ballistic motion of the wave packet center-of-mass (CoM) at roughly a mean free path ℓ , and then a symmetric localization of the packet around this new central position due to AL. We show in this Letter that the evolution is in fact very different. Quite unexpectedly, after an initial ballistic motion where the CoM indeed increases up to ℓ , the wave packet slowly *returns to its initial position*, recovering a symmetric shape at long times. The final state of the system is in turn identical to the one that would have been reached if no velocity had been transferred to the gas.

In this Letter, we thoroughly study this phenomenon both numerically and analytically. In dimension 1, we give an exact solution to this problem. We then study the CoM retroreflection in the presence of a weak nonlinearity describing particle interactions in the mean field approximation. The CoM freezes at a position that depends on the strength of interactions, very much like a decoherence process.

Let us consider a one-dimensional (1D) system described by the Hamiltonian $H = -\hbar^2 \Delta / (2m) + V(x)$, where $V(x)$ is a Gaussian, uncorrelated random potential: $\overline{V(x)} = 0$ and $\overline{V(x)V(x')} = \gamma \delta(x - x')$, where the overbar denotes averaging over disorder realizations. We wish to study the time evolution of a normalized Gaussian wave packet, $\Psi_{k_0}(x) \propto \exp[-x^2/(2\sigma^2) + ik_0x]$, to which a finite momentum $\hbar k_0$ is imprinted. We choose $k_0 > 0$ without loss of generality. To simplify the discussion, we assume throughout this Letter a sharp initial velocity distribution, $k_0\sigma \gg 1$, and weak disorder, $k_0\ell \gg 1$, thereby allowing for a simple description of the wave packet in terms of two velocity components $\pm \hbar k_0/m$, with energy $E_0 = \hbar^2 k_0^2 / (2m)$.

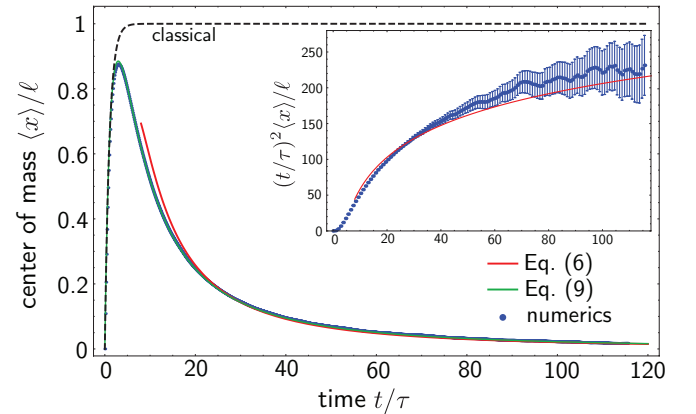


FIG. 1. (Color online) Main plot: center of mass as a function of time. Its long-time asymptotics, Eq. (6), is shown as a solid red curve, and the re-summation of the short-time series, Eq. (10), as a solid green curve. The latter perfectly overlaps with the numerical result (blue dots). The dashed curve is the classical result, Eq. (1). Inset: center of mass multiplied by $(t/\tau)^2$ as a function of time. The asymptotic result (6) (red curve) is compared to the numerical prediction, displayed with its statistical error bars. The parameters used in the simulations are given in the main text.

The average evolution in the random potential is governed by two microscopic scales, the scattering mean free time τ and the scattering mean free path $\ell = v_0\tau$, where

$v_0 = \hbar k_0/m$. Throughout this Letter, τ and ℓ are calculated to the leading order in $1/(k_0\ell) \ll 1$, using the Born approximation at energy E_0 [16]. The assumption of uncorrelated random potential is not crucial for our discussion: all the results that follow hold as well for short-range correlated potentials, provided that ℓ and τ are replaced by the transport mean free path and time, respectively [17, 18].

By numerically propagating $\Psi_{k_0}(x)$, we obtain the disorder-averaged density profile $|\overline{\Psi(x,t)}|^2$, from which we infer the CoM $\langle x \rangle \equiv \int x |\overline{\Psi(x,t)}|^2 dx$. The result is shown in Fig. 1: $\langle x \rangle$ first increases rapidly, reaches a maximum at $t \sim \tau$ and then slowly decreases to zero. In other words, after a transient motion rightward, the center of mass of the wave packet slowly *returns to its initial position* $x = 0$. For these simulations we discretize the Hamiltonian on a 1D grid of size $16000\pi/k_0$, divided into 251352 grid points. The initial wave-packet width is set to $\sigma = 10/k_0$, and $\gamma = 0.0058\hbar^4 k_0^3/m^2$ ($k_0\ell = \hbar^4 k_0^3/(2m^2\gamma) \simeq 86.5$). The results are averaged over 45000 disorder realizations. In the simulations, the evolution operator is expanded in a series of Chebyshev polynomials, as explained in [19, 20]. The surprising behavior observed in Fig. 1 is dramatically different from the classical expectation, which can be simply deduced from Ehrenfest theorem: $\partial_t \langle x \rangle_{\text{class}} = \langle p \rangle/m = \hbar k_0(n_+ - n_-)/m$ where n_{\pm} is the population of particles with momentum $\pm \hbar k_0$ ($n_+ + n_- = 1$). Using the classical Boltzmann equations $\partial_t n_{\pm} = (n_{\mp} - n_{\pm})/(2\tau)$ with the initial condition $n_+ = 0$, we find

$$\langle x \rangle_{\text{class}} = \ell \left(1 - e^{-t/\tau} \right), \quad (1)$$

which is shown in Fig. 1 as a dashed curve. Within the classical picture, the CoM thus quickly saturates to the mean free path ℓ , but never experiences retroreflection. The reason why quantum wave packets behave so differently can be understood by the following argument. At any time, the density distribution can be expanded over the eigenbasis $\{\epsilon_n, |\phi_n\rangle\}$ of H as

$$|\Psi(x,t)|^2 = \sum_{n,m} \langle \phi_n | \Psi_{k_0} \rangle \langle \Psi_{k_0} | \phi_m \rangle \times \phi_n(x) \phi_m^*(x) e^{-i(\epsilon_n - \epsilon_m)t}. \quad (2)$$

Since eigenstates are localized, the system is constrained to a volume set by the localization length $\xi = 2\ell$. This defines a typical mean level spacing $\Delta = 1/(\rho\xi)$ (ρ is the density of states per unit volume), with a corresponding localization time $\tau_{\text{loc}} = 2\pi\hbar/\Delta = 4\tau$ beyond which the off-diagonal oscillatory terms $n \neq m$ in Eq. (2) vanish, leaving:

$$|\overline{\Psi(x,\infty)}|^2 = \sum_n |\langle \phi_n | \Psi_{k_0} \rangle|^2 |\phi_n(x)|^2. \quad (3)$$

Due to time-reversal invariance, the $\phi_n(x)$ are real so that $\langle \phi_n | \Psi_{k_0} \rangle = \langle \phi_n | \Psi_{-k_0} \rangle^*$: Eq. (3) is independent of

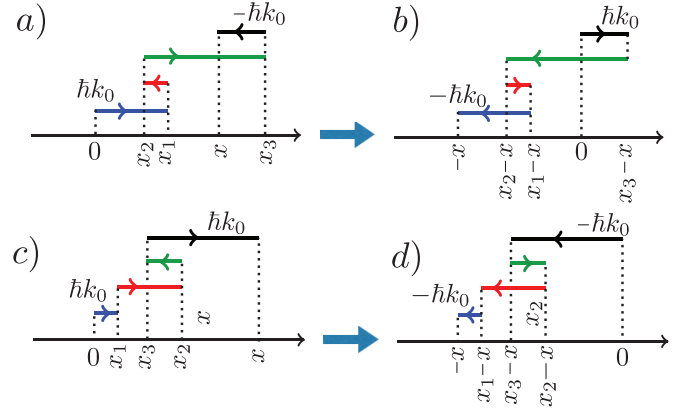


FIG. 2. a) A typical multiple scattering path going from $x = 0$ to x , contributing to $\langle x \rangle_-$ (the path is unfolded to the top for clarity). The momentum reverses at each scattering event. By time-reversing and translating this path by $-x$, we obtain path b), which gives an opposite contribution to $\langle x \rangle_-$, ensuring that $\langle x \rangle_-$ vanishes. c) Path contributing to $\langle x \rangle_+$. Its time-reversed and translated counterpart d) starts with momentum $-k_0$ and is thus not populated at $t = 0$, so that $\langle x \rangle_+ \neq 0$.

the sign of k_0 , and thus coincides with the long-time, spatially symmetric density distribution that would have been obtained with an initial wave packet having a symmetric velocity distribution. This shows that the CoM *must* return to its initial position at long times, as a result of AL.

Let us now be more quantitative and analyze the CoM at finite times. For this purpose, we start by applying Ehrenfest theorem to the mean-square displacement, $\partial_t \langle x^2 \rangle = \langle [x^2, p^2] \rangle / (2i\hbar m)$, and split the particle distribution into two classes of positive and negative velocities: $|\overline{\Psi(x,t)}|^2 = n_+(x,t) + n_-(x,t)$. This leads to [21]

$$\partial_t \langle x^2 \rangle = 2v_0 \langle x \rangle_+ - 2v_0 \langle x \rangle_- . \quad (4)$$

Here $\langle x \rangle_{\pm} = \int_{-\infty}^{\infty} x n_{\pm}(x,t) dx$, with obviously $\langle x \rangle = \langle x \rangle_+ + \langle x \rangle_-$. We now consider an arbitrary path contributing to $\langle x \rangle_-$ [Fig. 2(a)]. The path starts at $x = 0$ with momentum $\hbar k_0$ and reaches x with momentum $-\hbar k_0$ at time t . By time-reversing and translating this path of a distance $-x$, one can always find a complementary path starting with momentum $\hbar k_0$ at $x = 0$ and reaching $-x$ at time t (Fig. 2b). Due to time-reversal and translational invariance, these two paths contribute with the same weight to $n_-(x,t)$, which is thus an even function of x , yielding $\langle x \rangle_- = 0$. This reasoning does not apply to $\langle x \rangle_+$ since the time-reversed/translated counterpart of an arbitrary path contributing to $\langle x \rangle_+$ starts by construction with a momentum $-\hbar k_0$ which is not initially populated (see Figs. 2c-d). We have thus

$$\partial_t \langle x^2 \rangle = 2v_0 \langle x \rangle, \quad (5)$$

a property that we can use to infer the long-time limit of $\langle x \rangle$ from $\langle x^2 \rangle$, which was previously studied in [22]. This yields [23]

$$\langle x \rangle = \ell \frac{64 \ln(t/4\tau) \tau^2}{t^2} + \mathcal{O}\left(\frac{1}{t^2}\right). \quad (6)$$

Eq. (6) is shown in Fig. 1 and matches well the exact numerical prediction at long times. The inset of Fig. 1 also confirms the presence of the logarithmic term in Eq. (6).

In fact, one can go one step further and exploit Eq. (5) to compute $\langle x \rangle$ at *any time*. For this purpose, we use Berezinskii diagrammatic technique [24] which, combined with Eq. (5), gives [23]

$$\langle x \rangle = \int \frac{d\omega}{2\pi} e^{-i\omega t} \left[-\frac{2\ell}{i\omega} \sum_{m=0}^{\infty} P_m^1(\omega) Q_m^1(\omega) \right], \quad (7)$$

where $P_m^1(\omega) = s\Gamma(m+1)[\Psi(m+1, 2; -s) - (m+1)\Psi(m+2, 2; -s)]$, with $s = 4i\omega\tau$, Γ the Gamma function and Ψ the confluent hypergeometric function of the second kind. The $Q_m^1(\omega)$ are solutions of

$$[4i\tau(m+1/2)\omega - (m+1)^2 - m^2]Q_m^1(\omega) + (m+1)^2 Q_{m+1}^1(\omega) + m^2 Q_{m-1}^1(\omega) + P_m^1(\omega) = 0. \quad (8)$$

At short times, one can solve these equations with the expansion $Q_m^1(\omega) = \sum_{n=0}^{+\infty} q_{m,n}/(i\omega)^n$. To compute the $q_{m,n}$, we first notice that $q_{m,i} = 0$ if $i \leq m$, which follows from the large-frequency expansion of $P_m^1(\omega)$ (which has no terms $1/\omega^i$ with $i < m$). We use this result to expand Eqs. (8) order by order in $1/\omega$ and reduce them to a triangular system. This method provides us with the coefficients χ_n of the expansion $\langle x \rangle = \ell \sum_n \chi_n (t/\tau)^n$ at arbitrary order [18]. We find for instance

$$\langle x \rangle = \ell \left[\frac{t}{\tau} - \frac{t^2}{2\tau^2} + \frac{t^3}{6\tau^3} - \frac{3t^4}{64\tau^4} \right] + \mathcal{O}(t^5). \quad (9)$$

The method cannot be directly used to estimate $\langle x \rangle$ at any time because the series has a finite convergence radius, estimated at 4τ from the first 100 terms. Nevertheless, the observed exponential decay of the χ_n makes this series a good candidate for a Padé resummation. The knowledge of the long-time limit (6) suggests to express the CoM at any time under the form

$$\langle x \rangle = \ell \frac{\ln(1+t/4\tau) \tau^2}{t^2} \lim_{n \rightarrow \infty} R_n(t), \quad (10)$$

where $R_n(t)$ is a diagonal Padé approximant of order n , deduced from the χ_n coefficients [25]. In practice, $R_n(t)$ converges quickly, and an excellent approximation of $\langle x \rangle$ for times up to 120τ is obtained with $n = 7$. This is demonstrated by the solid green curve in Fig. 1, which perfectly coincides with the numerical results.

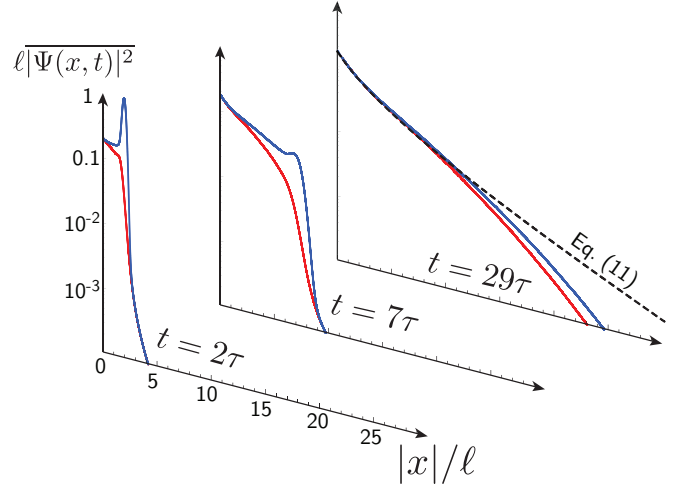


FIG. 3. (Color online) Average density profile obtained numerically at three different times. The solid upper blue and lower red curves are the $x > 0$ and $x < 0$ components of the profile, respectively. The long-time limit of the profile, Eq. (11), is shown as a dashed black curve.

In order to clarify which specific behavior of the spatial distribution $|\Psi(x, t)|^2$ actually gives rise to the phenomenon of retroreflection, we show in Fig. 3 the $x > 0$ (blue curve) and $x < 0$ (red curve) components of the spatial profile $|\Psi(x, t)|^2$, obtained numerically at three successive times. The profiles display a ballistic peak responsible for the increase of $\langle x \rangle$ at short times. After this peak has been attenuated, the profile re-symmetrizes itself around $x = 0$, which gives rise to the retroreflection phenomenon. As discussed above, this distribution is expected to converge toward a symmetric one, Eq. (3), which coincides with the so-called Gogolin density profile [17, 26]:

$$|\overline{\Psi(x, \infty)}|^2 = \int_0^\infty \frac{d\eta \pi^2}{32\ell} \frac{\eta (1 + \eta^2)^2 \sinh(\pi\eta) e^{-(1+\eta^2)|x|/8\ell}}{[1 + \cosh(\pi\eta)]^2}, \quad (11)$$

which is shown in Fig. 3 for comparison. Note that although we start from a rather narrow wave packet with $\sigma < \ell$ in our simulations, the retroreflection phenomenon is present as well when $\sigma > \ell$.

We finally discuss the effect of particle interactions on $\langle x \rangle(t)$, by considering a weakly interacting, condensed bosonic gas. Its dynamics is governed, at the mean field level, by the Gross-Pitaevskii equation $i\hbar \partial_t \Psi = [-\hbar^2 \Delta/2m + V(x) + g|\Psi|^2]\Psi$. For wave packets with $k_0 = 0$, it was shown that the interaction term $g|\Psi|^2$ leads to a destruction of AL at very long times, in favor of a regime of subdiffusion where $\langle x^2 \rangle \sim t^\alpha$ with $\alpha < 1$ [27, 28]. Here we take a different perspective and investigate numerically how the nonlinearity affects $\langle x \rangle$. For these simulations, we write the evolution operator over a small time step

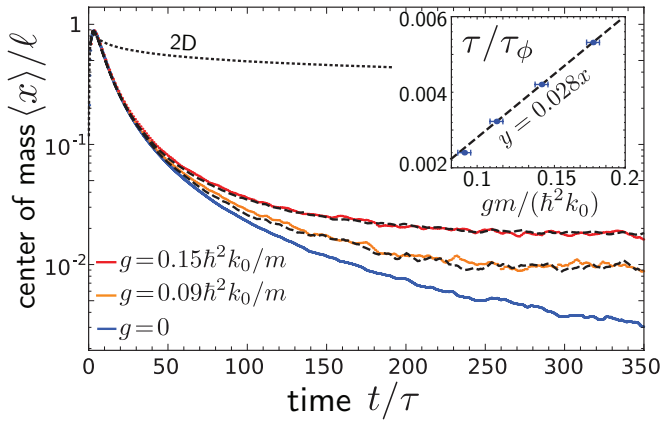


FIG. 4. (Color online) Main plot: center of mass $\langle x \rangle_g$ as a function of time, for $g = 0$ (solid lower blue curve), $g = 0.09\hbar^2 k_0/m$ (solid middle orange curve) and $g = 0.15\hbar^2 k_0/m$ (solid upper magenta curve). Two dashed curves show the center of mass $\langle x \rangle_\phi$ obtained with the model of decoherence, for $A_f = 0.02, 0.03$. Dotted curve: CoM in 2D. Inset: $\tau/\tau_\phi(g)$, well fitted by a linear regression. The effective decoherence time $\tau_\phi(g)$ associated with the nonlinearity thus behaves like $\hbar/\tau_\phi(g) \sim g/\ell$.

δt as $U(\delta t) = \exp[-ig|\Psi(\delta t)|^2 \delta t/2] \exp[-i(-\hbar^2 \Delta/2m + V)\delta t] \exp[-ig|\Psi(0)|^2 \delta t/2]$ and treat the linear part as before, through an expansion in a series of Chebyshev polynomials. We use a system of size $7500\pi/k_0$ discretized into 23562 grid points, and propagate a wave packet of width $\sigma = 10/k_0$ in a random potential of strength $\gamma = 0.0196\hbar^4 k_0^3/m^2$ ($k_0\ell \simeq 18.1$). The results are averaged over 600000 (8.85 millions) disorder realizations when $g \neq 0$ (respectively $g = 0$). We show in Fig. 4 the CoM $\langle x \rangle_g$ as a function of time obtained with this procedure, for two values of $g \neq 0$. We observe that $\langle x \rangle_g$ decreases more slowly than in the non-interacting limit and saturates at a finite value at long times. The CoM retroreflection is thus interrupted by the nonlinearity.

To better understand the role of the nonlinearity, we have also studied how the CoM is affected by *decoherence*, modeled by the Hamiltonian $H = -\hbar^2 \Delta/(2m) + V(x) + V_\phi(x, t)$. Here $V(x)$ is the same random potential as above and $V_\phi(x, t) = \hbar(x)f(t)$, where $h(x)$ has the same statistical properties as $V(x)$ and $f(t)$ is a random, Gaussian distributed function of time with zero average. $f(t)$ is fully characterized by its time-time correlation function which we choose Gaussian, $f(t)f(t') = A_f^2 \exp[-(t-t')^2/2\sigma_t^2]$, with $A_f \ll 1$ to ensure that the fluctuating potential is weaker than the static one. We have checked that the potential $V_\phi(x, t)$ does induce decoherence: at long times, it restores classical diffusion with $\langle x^2 \rangle = 2D_\phi t$, where $D_\phi = \xi^2/\tau_\phi = 4\ell^2/\tau_\phi$ is the diffusion coefficient and τ_ϕ the decoherence time [17]. Because $V_\phi(x, t)$ preserves time-reversal and translational invari-

ance after a disorder average, Eq. (5) still holds for this model, demonstrating that the CoM, $\langle x \rangle_\phi$, converges to a finite value $4\ell\tau/\tau_\phi$ at long times. $\langle x \rangle_\phi$ is displayed in Fig. 4 (dashed curves), for two values of A_f . The two values of g chosen in the Gross-Pitaevskii model were adjusted so that $\langle x \rangle_g$ coincides with these two curves $\langle x \rangle_\phi$ in the long-time limit. Surprisingly, the obtained curves $\langle x \rangle_\phi$ match extremely well the nonlinear curves $\langle x \rangle_g$ in the whole time window. This suggests that at least regarding $\langle x \rangle$ and for times short enough for subdiffusion not to play a major role, the nonlinearity acts similarly to a decoherence process. From this observation, we associate to the nonlinearity an effective decoherence time $\tau_\phi(g)$. To find this quantity, we first determine D_ϕ from the evolution of $\langle x^2 \rangle$ with time in the model of decoherence, and then find the associated g by matching the curves $\langle x \rangle_\phi$ and $\langle x \rangle_g$ at long time. The results, shown in the inset of Fig. 4, demonstrate that $\hbar/\tau_\phi(g) \propto g/\xi$, which can be interpreted as the average interaction energy within a localization volume $\xi = 2\ell$. A similar time scale for the dynamical alteration of localization by interactions was found in [29, 30].

We expect the retroreflection phenomenon to be a rather general property of systems displaying Anderson localization. In particular, it is not restricted to 1D systems, as can be inferred from a straightforward extension to any dimension of the reasoning leading to Eq. (3). We have also numerically checked that the CoM indeed goes back to its initial position in two-dimensional (2D) random potentials, see the dotted curve in Fig. 4, obtained using the 2D version of the potential $V(x)$ (with $k_0\ell \simeq 2.5$). At weak disorder, the decay of $\langle x \rangle(t)$ is however much slower in 2D because the localization time is much longer than in 1D. The fact that the retroreflection is significantly affected by weak interactions at short times suggests that it could be advantageously used as a sensitive probe of Anderson localization in interacting disordered systems.

We thank Christian Miniatura for discussions at the early stages of this work.

-
- [1] P. W. Anderson, Phys. Rev. **109**, 1492 (1958).
 - [2] A. A. Chabanov, M. Stoytchev, and A. Z. Genack, Nature **404**, 850 (2000).
 - [3] T. Schwartz, G. Bartal, S. Fishman, and M. Segev, Nature **446**, 52 (2007).
 - [4] M. Störzer, P. Gross, C. M. Aegerter, and G. Maret, Phys. Rev. Lett. **96**, 063904 (2006).
 - [5] T. Sperling, L. Schertel, M. Ackermann, G. J. Aubry, C. M. Aegerter, and G. Maret, New J. Phys. **18**, 013039 (2016).
 - [6] H. Hu, A. Strybulevych, J. H. Page, S. E. Skipetrov, and B. A. Van Tiggelen, Nature Phys. **4**, 945 (2008).
 - [7] J. Chabé, G. Lemarié, B. Grémaud, D. Delande, P. Szriftgiser, and J. C. Garreau, Phys. Rev. Lett. **101**, 255702 (2008).

- (2008).
- [8] J. Billy, V. Josse, Z. Zuo, A. Bernard, B. Hambrecht, P. Lugan, D. Clément, L. Sanchez-Palencia, P. Bouyer, and A. Aspect, *Nature* **453**, 891 (2008).
 - [9] F. Jendrzejewski, A. Bernard, K. Müller, P. Cheinet, V. Josse, M. Piraud, L. Pezzé, L. Sanchez-Palencia, A. Aspect, and P. Bouyer, *Nature Phys.* **8**, 398 (2012).
 - [10] I. Manai, J. F. Clément, R. Chicireanu, C. Hainaut, J. C. Garreau, P. Szriftgiser, and D. Delande, *Phys. Rev. Lett.* **115**, 240603 (2015).
 - [11] G. Semeghini, M. Landini, P. Castilho, S. Roy, G. Spagnolli, A. Trenkwalder, M. Fattori, M. Inguscio, and G. Modugno, *Nature Phys.* **11**, 554 (2015).
 - [12] M. Schreiber, S. S. Hodgman, P. Bordia, H. P. Lüschen, M. H. Fischer, R. Vosk, E. Altman, U. Schneider, and I. Bloch, *Science* **349**, 842 (2015).
 - [13] J. Choi, S. Hild, J. Zeiher, P. Schauß, A. Rubio-Abadal, T. Yefsah, V. Khemani, D. A. Huse, I. Bloch, and C. Gross, *Science* **352**, 1547 (2016).
 - [14] G. Modugno, *Rep. Prog. Phys.* **73**, 102401 (2010).
 - [15] B. Shapiro, *J. Phys. A: Math. Theor.* **45**, 143001 (2012).
 - [16] E. Akkermans and G. Montambaux, *Mesoscopic physics of electrons and photons* (Cambridge University Press, 2007).
 - [17] A. A. Gogolin, *Physics Reports* **86**, 1 (1982).
 - [18] T. Prat, D. Delande, and N. Cherroret, to be published.
 - [19] S. Roche and D. Mayou, *Phys. Rev. Lett.* **79**, 2518 (1997).
 - [20] H. Fehske, J. Schleede, G. Schubert, G. Wellein, V. S. Filinov, and A. R. Bishop, *Phys. Lett. A* **373**, 2182 (2009).
 - [21] This can be justified more rigorously by using the phase space Wigner representation $\overline{W}(x, p, t)$ of the wave packet. In the weak-disorder approximation, $\overline{W}(x, p, t)$ is non vanishing only near $p = \pm \hbar k_0$, so that it can be split in two parts $\overline{W}(x, p, t) \approx n_+(x, t)\delta(p - \hbar k_0) + n_-(x, t)\delta(p + \hbar k_0)$.
 - [22] E. P. Nakhmedov, V. N. Prigodin, and Yu. A. Firsov, *Zh. Eksp. Teor. Fiz.* **92**, 2133 (1987) [*Sov. Phys. JETP* **65**, 1202 (1987)].
 - [23] Although the calculations in [22, 24] are correct, there are occasionally factors 2 missing in some equations.
 - [24] V. L. Berezinsky, *Zh. Eksp. Teor. Fiz.* **65**, 1251 (1973) [*Sov. Phys. JETP* **38**, 620 (1974)].
 - [25] G. A. Baker Jr., *Essentials of Padé Approximants*, Academic Press (New York).
 - [26] To obtain Eq. (11), one starts from $\Psi_{k_0}(x) \propto \exp(-x^2/2\sigma^2)\cos(k_0x)$, i.e. from a state having a momentum distribution symmetric with respect to $k = 0$.
 - [27] M. Mulansky, K. Ahnert, A. Pikovsky, and D. L. Shepelyansky, *Phys. Rev. E* **80**, 056212 (2009).
 - [28] S. Flach, *Springer Proc. Phys.* **173**, 45 (2016).
 - [29] A. Iomin, *Phys. Rev. E* **81**, 017601 (2010).
 - [30] N. Cherroret, *J. Phys.: Condens. Matter* **29**, 024002 (2017).